Journal of
Applied Crystallography

ISSN 0021-8898

Received 12 July 2012
Accepted 21 November 2012

Grazing-incidence transmission X-ray scattering: surface scattering in the Born approximation

Xinhui Lu,[a]‡ Kevin G. Yager,[b]* Danvers Johnston,[b] Charles T. Black[b] and Benjamin M. Ocko[a]*

[a]Condensed Matter Physics and Materials Science Department, Brookhaven National Laboratory, Upton, NY 11973, USA, and [b]Center for Functional Nanomaterials, Brookhaven National Laboratory, Upton, NY 11973, USA. Correspondence e-mail: kyager@bnl.gov, ocko@bnl.gov

Determination of the three-dimensional order in thin nanostructured films remains challenging. Real-space imaging methods, including electron microscopies and scanning-probe methods, have difficulty reconstructing the depth of a film and suffer from limited statistical sampling. X-ray and neutron scattering have emerged as powerful complementary techniques but have substantial data collection and analysis challenges. This article describes a new method, grazing-incidence transmission small-angle X-ray scattering, which allows for fast scattering measurements that are not burdened by the refraction and reflection effects that have to date plagued grazing-incidence X-ray scattering. In particular, by arranging a sample/beam geometry wherein the scattering exits through the edge of the substrate, it is possible to record scattering images that are well described by straightforward (Born approximation) scattering models.

1. Introduction

Nanostructured thin films are of interest in microelectronics, photonics and bioengineering, yet quantifying their three-dimensional structure remains challenging (Park, 2009; Yan & Yang, 2009). Grazing-incidence small-angle X-ray scattering (GISAXS) is a reflection-mode technique well suited to organic and hybrid nanomaterial thin films since it is surface and subsurface sensitive, nondestructive, and compatible with *in situ* measurements (Levine *et al.*, 1989; Doshi, 2003; Renaud *et al.*, 2009; Rauscher, 1999; Bian *et al.*, 2011; Papadakis *et al.*, 2008; Zhang *et al.*, 2012). However the analysis of GISAXS data is severely complicated by strong refraction effects, which distort reciprocal space, and intense reflection effects, which give rise to multiple terms in the scattering equation, whose interference is nontrivial (Busch *et al.*, 2006). In a serendipitous series of experiments, we observed strong and undistorted scattering patterns emerging below the substrate horizon, in cases where the sample and beam were near the edge of the substrate. Subsequently, we have formalized this into a robust technique: grazing-incidence transmission small-angle X-ray scattering (GTSAXS), wherein a monochromatic X-ray beam is focused onto the edge of a nanostructured thin film. Appropriate geometry enables recovery of the undistorted scattering pattern. GTSAXS retains the sensitivity to lateral and perpendicular film structure and the strong signal and fast data acquisition of GISAXS, while reducing (for all practical purposes eliminating) the multiple scattering/refraction issues associated with typical grazing-incidence analysis. This study complements very recent grazing-incident-angle neutron scattering measurements and analysis (Busch *et al.*, 2011) which utilized the same geometrical concepts that we present here for X-rays. Despite the higher absorption with X-rays than with neutrons, we show that GTSAXS is a feasible and robust surface scattering geometry when sufficiently focused beams and energetic X-rays are utilized.

GISAXS was introduced by Levine *et al.* in 1989 to study the dewetting of gold deposited on glass surfaces. It has since become a very popular method for many surface and subsurface studies, including polymers, nanoparticles and quantum dots (Lin, 2005; Urban *et al.*, 2006; Hlaing *et al.*, 2011; Jiang *et al.*, 2011). In a typical grazing-incidence experiment, the scattering below the horizon is strongly attenuated because of the long path length for scattering at shallow angles, and in a GISAXS measurement only the scattering above the horizon is considered. Quantitative analysis of the above-horizon scattering typically requires careful consideration of refraction and reflection interference. However, when the incident angle is sufficiently large the scattering can be successfully described within the quasi-kinematic approximation (Heitsch *et al.*, 2010; Smilgies *et al.*, 2012), where the surface enhancement is confined to the Vineyard (1982) factor and multiple scattering is minimal and hence ignored. A limitation of such large-incident-angle GISAXS measurements is that it is not possible to probe q_z close to zero (Roth *et al.*, 2003, 2007, 2011). To include multiple scattering either the distorted wave Born approximation (Sinha *et al.*, 1988; Rauscher *et al.*, 1995; Busch *et al.*, 2006; Lee *et al.*, 2005, 2007) or the more complicated graded distorted wave Born approximation (Lazzari *et al.*, 2007; de Boer, 1996; Sentenac &

‡ Present address: Department of Physics, The Chinese University of Hong Kong, Shatin, Hong Kong, People's Republic of China.

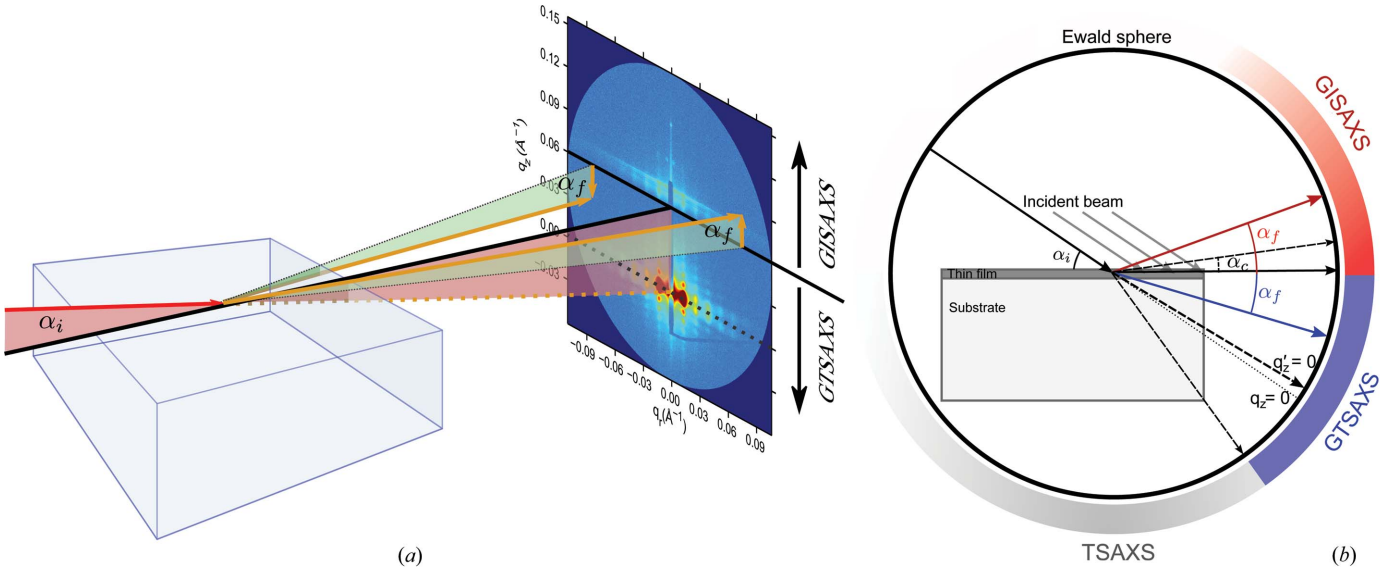

Figure 1
(*a*) A three-dimensional illustration of GTSAXS and GISAXS geometries. The incident beam (red arrow) impinges on the sample at a grazing angle of α_i and the scattered beam is collected by an area detector. The direct incoming beam (orange dotted line) goes through the origin of the q_r–q_z reciprocal space. In the scattering image, the solid line $[q_z = (2\pi/\lambda)\sin\alpha_i]$ marks the surface horizon, which divides the whole scattering image into the GTSAXS and GISAXS regimes. The dotted line corresponds to the direct beam ($q_z = 0$). (*b*) A two-dimensional Ewald sphere illustration of the GTSAXS, GISAXS and TSAXS regimes. The rather large grazing incident angle shown is for illustrative purpose. In GISAXS measurements α_i is close to grazing incidence and in TSAXS the range is typically $20 \leq \alpha_i \leq 90^\circ$.

Greffet, 1998) is typically used. An alternative is to use transmission small-angle X-ray scattering (TSAXS) (Tate *et al.*, 2006), in particular the critical dimension (CDSAXS) variant (Jones, 2003; Hu, 2004). In this technique the X-rays transit through the front and back faces of the sample and substrate. However, in order to probe large surface-normal scattering vectors, multiple detector images must be acquired at many different tilt angles. This reconstruction of reciprocal space is time consuming and still cannot fully determine the surface-normal structure. GTSAXS thus represents a unique blending of the advantages of GISAXS (fast measurements, which include film-normal information) and TSAXS (scattering unperturbed by complicated corrections) and is capable of probing very small q_z and also negative q_z, both of which are not possible with GISAXS. Hence, GTSAXS is particularly well suited to investigating structural features when the film thickness is comparable to the inverse-surface-normal scattering vector magnitude (about 20 nm for silicon). To validate this methodology, we present scattering data for two well defined samples. We first present data for fingerprint trenches that are randomly oriented (in-plane powder). We then demonstrate the applicability to anisotropic materials by quantifying the scattering from a line grating.

2. GTSAXS geometry

Fig. 1(*a*) illustrates the three-dimensional geometry for GTSAXS and GISAXS. In both geometries the X-rays are incident on the sample surface with a grazing angle α_i and with an exit angle α_f. By convention, α_i and α_f are positive when the beam enters or exists from the top surface. The surface-normal scattering vector magnitude is $q_z = k_0(\sin\alpha_i + \sin\alpha_f)$, where $k_0 = 2\pi/\lambda$ and λ is the wavelength of the X-rays. In Fig. 1(*a*), the solid line designates the boundary between the GISAXS and GTSAXS regimes. In the GISAXS regime $\alpha_f > 0$ and the scattering is above the horizon; in the GTSAXS regime $\alpha_f < 0$ and the scattered rays are below the horizon. In GTSAXS, the scattering exits through the far edge of the sample (see Fig. 1*b*) and not through the bottom of the sample, as it would in TSAXS.

To minimize the loss of signal due to sample absorption, the area of interest should extend close to the edge of the sample and this area must be illuminated. Under optimal conditions, the footprint of the beam on the sample (L) should be smaller than the X-ray absorption length in the substrate (ξ). If on the other hand the opposite condition exists (the present case) then absorption decreases the scattering intensity by a factor of $\sim\xi/L$. In this case the effective footprint on the sample is ξ. We note that in this geometry the dependence of the absorption on α_i and α_f represents a minor correction, which we will ignore (see supplementary material[1]). In typical grazing-incidence measurements the center of the sample is illuminated; substrate absorption extinguishes the GTSAXS signal. Having the scattering exit from the edge of the sample, rather than from the top, substantially reduces the multiple scattering events that complicate GISAXS data analysis, especially at small surface-normal scattering vectors (discussed below). In contrast to TSAXS, where the absorption increases with q_z, for GTSAXS the absorption is essentially q_z independent. In the two-dimensional detector images

[1] Supplementary information is available from the IUCr electronic archives (Reference: DB5107). Services for accessing this material are described at the back of the journal.

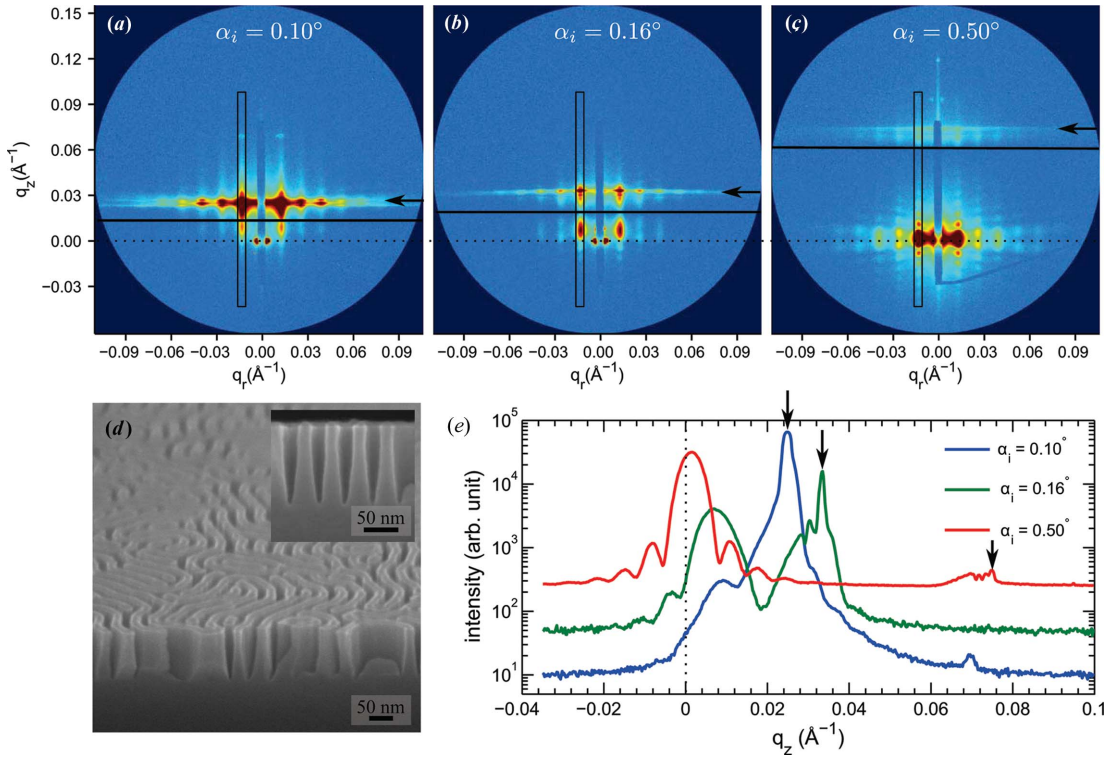

Figure 2
Scattering images of lamellar-type silicon nanostructures at incident angles of (*a*) 0.10°, (*b*) 0.16° and (*c*) 0.50°. The direct beam position and the surface horizon position are denoted by dotted and solid lines, respectively. (*d*) A SEM image of the silicon nanostructure. The inset shows the cross-sectional SEM image. (*e*) Scattering profiles for the first-order BRs, obtained from the boxed regions in (*a*)–(*c*).

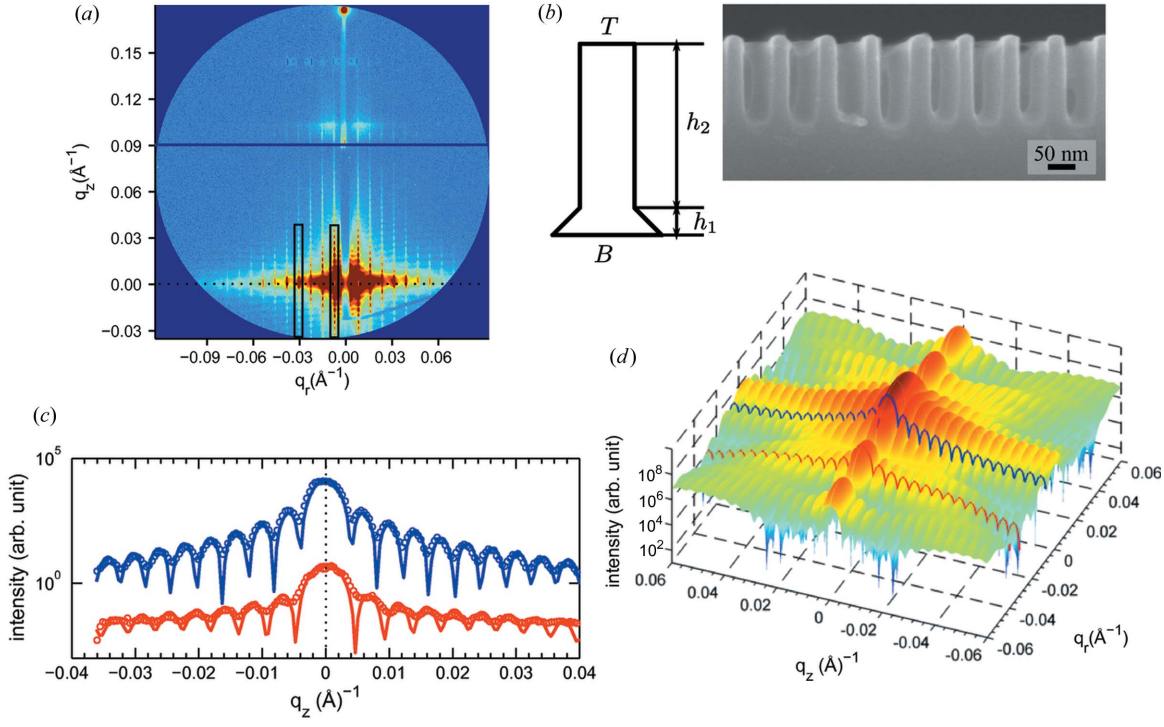

Figure 3
(*a*) Scattering images of a silicon grating at an incident angle of $\alpha_i = 0.76°$. The direct beam position ($q_z = 0$) and the surface horizon position ($\alpha_f = 0$) are denoted by the black dotted line and the blue solid line, respectively. (*b*) A cross-sectional SEM view of the grating. It is modeled by a rectangular shape with a trapezoidal bottom. (*c*) The intensity profile along q_z of first- (blue) and fourth-order (red) BRs [taken from the rectangular areas marked in panel (*a*)], fitted with the corresponding form factor (solid lines). (*d*) A three-dimensional representation of the form factor of the modeled shape shown in panel (*b*).

in Figs. 1–3, we show two lines at fixed q_z. The dotted line corresponds to the direct-beam condition (*i.e.* $q_z = 0$) and the solid line corresponds to the surface horizon (*i.e.* $\alpha_f = 0$). Owing to refraction effects associated with α_i (see Fig. 1*b*), the direct beam is shifted slightly when the substrate is in place.

3. X-ray scattering measurements

The GTSAXS and GISAXS experiments were performed at the X9 undulator beamline at the National Synchrotron Light Source, Brookhaven National Laboratory, where the 13.5 keV photons ($\lambda = 0.9184$ Å) are focused to a spot with a height of ~50 µm and a width of 200 µm at the sample position. At an incident angle five times the critical angle (0.66°), a typical incident angle for these measurements, about 10% of the scattered beam is transmitted to the edge of the sample. The optimal vertical beam size (~4µm) at this energy is somewhat beyond the best possible vertical focus at X9 (10 µm). Despite the absorption losses, the results presented below still show strong signal, pointing to the general applicability of GTSAXS. Higher-energy X-rays would provide a larger effective footprint, taking into account the reduced critical angle and the increased absorption length.

The scattering/sample chamber vacuum was maintained at $\sim 10^{-2}$ Torr (1 Torr = 133 Pa) in order to reduce beam damage, diffuse scattering and X-ray absorption. A two-dimensional CCD detector was placed ~5.4 m from the sample to collect the small-angle X-ray scattering images. Scattering features in the q_z direction correspond to the out-of-plane structure of the sample, while those in the q_r direction correspond to in-plane structure. φ is defined as the azimuthal angle between the grating grooves and the plane of the incident beam (the pink plane in Fig. 1). As Yan & Gibaud (2007) have pointed out for the GISAXS geometry, the Ewald sphere only intersects Bragg rods at a single point, arranged on a semicircle, when φ is fixed. Rueda *et al.* (2012) also observed a semicircular arrangement for hard gratings in contrast to the Bragg rod-like patterns they found for soft-matter gratings. For our samples, in order to collect Bragg rods it is required to sweep the Ewald sphere by rotating φ at a constant rate over a finite angular range. Alternatively CCD images could be acquired at hundreds of evenly spaced values of φ accompanied by appropriate analysis. We chose to use the former approach and to accomplish this during our measurement the grating was rotated over a ±6° range of φ at a constant speed of 1.2° per second (Hofmann *et al.*, 2009) while the image was collected (10 s integration time). This same approach has been used by our group to study nanoimprinted samples (Hlaing *et al.*, 2011, 2012). A rotation was not required for the fingerprint patterns that exhibit an in-plane powder behavior.

4. Results

As an example of a canonical nanostructured thin film, we present results for a fingerprint pattern obtained by etching a block-copolymer perpendicular-lamellar structure into silicon [see scanning electron microscopy (SEM) images in Fig. 2(*d*)]. The sample preparation details are described in Appendix *A*. The in-plane alignment of the lamellae is isotropic so that the scattering is independent of the azimuthal angle. Fig. 2 presents X-ray scattering images for three different incident angles. The critical angle of silicon at 13.50 keV is $\alpha_{Si} = 0.132°$. At $\alpha_i = 0.10°$, an angle less than α_{Si}, the X-rays only evanescently probe the silicon substrate, as a result of total external reflection. At $\alpha_i = 0.16$ and 0.50° the X-rays fully penetrate the substrate.

All three images show vertical scattering streaks, commonly referred to as Bragg rods (BRs) (Guinier, 1994). These rods are evenly separated in plane by $\Delta q_r = 0.0134 \pm 0.0001$ Å^{-1}, consistent with the SEM measurement of a one-dimensional system with a single lattice constant of 469 Å. The scattering profiles for the first-order BR are shown in Fig. 2(*e*); these were obtained from the scattering images in Figs. 2(*a*)–2(*c*).

In a GISAXS measurement one typically sets the incident angle close to, but larger than, the critical angle of the least dense material. This condition gives the largest range of positive q_z, allows full penetration of the surface and maximizes the electric field in the sample, hence maximizing the scattering intensity. To reduce multiple scattering effects and to decrease the footprint size on the sample, some studies have successfully utilized incident angles of about five times the critical angle (Roth *et al.*, 2003, 2009, 2011), albeit with a restricted range at small q_z. When α_f is close to α_{Si} the scattering is also enhanced because of the increased field and this gives rise to the horizontal streak of scattering in the images associated with the so-called Vineyard (Yoneda) peak (Yoneda, 1963). The positions of these streaks are indicated by the arrows in Figs. 2(*a*)–2(*c*) and 2(*e*). The presence of the Vineyard peak in the GISAXS regime and the absence of it in the GTSAXS regime in part simplifies the analysis of GTSAXS data.

The scattering pattern for $\alpha_i = 0.50°$, an angle considerably larger than α_{Si}, clearly shows the presence of multiple modulation peaks for the lowest-order BRs in the GTSAXS regime. The modulation results from the q_z component of the form factor of the fingerprint pattern, where in principle the analysis of the BRs allows the determination of the average shape of the etched grooves. No q_z modulation peaks are observed in the GISAXS regime for any of the three α_i values. The presence of the well defined BR modulations in the GTSAXS regime at a high grazing incident angle is an inherent advantage of this geometry.

A detailed comparison of the lowest-order BRs at different α_i, shown in Fig. 2(*e*), provides additional insight. At $\alpha_i = 0.50$ (red curve) and 0.16° (green curve) BR modulations are evident. At 0.16° the BR modulation is only apparent for negative q_z since for positive q_z it extends into the GISAXS regime. In contrast, the BR for $\alpha_i = 0.50°$ is rather symmetric around $q_z = 0$, as expected from simple scattering theory. The period of the BR modulation, Δq_z, is equal to 0.0067 Å^{-1}. For an etched pattern with flat tops and bottoms, the pattern depth h is equal to $2\pi/\Delta q_z$ and this corresponds to $h = 938$ Å, which is close to the value obtained with SEM. The small difference is due to the triangular shape of the grooves, and in principle

shape details could be determined through more detailed BR analysis.

As Fig. 2(*e*) clearly demonstrates, for $\alpha_i = 0.50^\circ$ the Vineyard peak ($\sim$0.075 Å^{-1}) is far from $q_z = 0$ where the interesting BR modulations are the strongest. At $\alpha_i = 0.16^\circ$ the Vineyard peak ($\sim$0.040 Å^{-1}) complicates the scattering for $q_z > 0$. It is the presence of the Vineyard peak, along with the associated strong refraction effects, that obscures and limits the interpretation of many GISAXS measurements. In part, this is because the Vineyard peak only has a well defined shape for the simplest density profiles. This example demonstrates that the BRs in the GTSAXS regime, with their symmetric shape, are not significantly influenced by the strong reflection and refraction effects that dominate in the GISAXS regime.

We note that refraction is not entirely absent in GTSAXS. The position of the direct beam, in the absence of the sample, is defined by the intersection of the q_z and q_r axes. A small fraction of the direct beam passes over the top of the sample and shows up on either side of the vertical beamstop, near the origin. The beam transmitted through the sample is slightly refracted, which also causes the GTSAXS scattering pattern to be shifted slightly from $q_z = 0$; the refraction is greatest for small α_i. As we present quantitatively below, however, the refraction correction in GTSAXS is small and well behaved. Corrections to account for substrate absorption and Ewald curvature are negligible (see supplementary information).

We carried out GTSAXS studies on a well aligned high-aspect-ratio silicon grating: representative of highly ordered anisotropic samples. The sample preparation details are described in Appendix *A*. The GTSAXS pattern obtained at $\alpha_i = 0.76^\circ$, shown in Fig. 3(*a*), was collected while the sample was rotated at a constant rate over a 12° range of azimuthal angles (see §3 for details). The pattern exhibits many BRs where all of the low-order rods exhibit strong modulations (12 periods for the lowest-order rod), a characteristic of strong interference between the top and bottom surfaces of the grating. The spacing between each BR is 0.0079 Å^{-1}, indicating a grating periodicity of 795 Å, consistent with the cross-sectional SEM results presented in Fig. 3(*b*). This scattering pattern is symmetric about $q_r = 0$ and nearly symmetric about $q_z = 0$. In the case of GISAXS studies of similar patterns (Hofmann *et al.*, 2009; Hlaing *et al.*, 2011) the BRs are always entangled with the Vineyard peak at low q_z along with the associated strong refraction/reflection effects near the critical angle, thus requiring the use of complex scattering models.

The intensities of the BRs in the GTSAXS regime were calculated using the Born approximation where the intensity scales as the form factor modulus squared. Whereas the sinc function [$\sin(x)/x$] form factor – exact for rectangular-shaped grooves – provides an adequate description of the first BR, it fails to describe the positions and intensities of the higher-order rods correctly. To analyze the results, we used a 'footed' rectangular cross section, illustrated in Fig. 3(*b*), to calculate the form factor. Of course, a more refined description of the cross section would provide a better description of the Bragg rods but this is beyond the scope of the present manuscript. The modeled three-dimensional form factor is presented in Fig. 3(*d*). The intensity profiles along the first-order and fourth-order BRs (q_r = 0.0079 and 0.031 Å^{-1}) are plotted in blue and red circles, respectively, in Fig. 3(*c*). This calculation includes a small refraction correction, discussed in detail below. The modeled shape provides an excellent description of the Bragg rods [blue and red curves in Figs. 3(c) and 3(*d*)] with a rectangle width T = 300 Å, a foot width B = 660 Å, and heights $h_1 + h_2$ = 1570 Å and h_1 = 210 Å. This simple shape is able to capture the essential features of two BRs. Because the two-dimensional form factor data are undistorted and uncomplicated, they could be fitted in detail to extract arbitrary information about the cross section: *e.g.* the curvature of the top and bottom grooves.

5. Discussion

The distorted wave Born approximation (DWBA) (Sinha *et al.*, 1988; Rauscher *et al.*, 1995; Busch *et al.*, 2006) is often used to model GISAXS data. Typically two slabs of constant densities are considered: a top slab where the scattering events take place and a substrate slab which contributes to reflectivity. For more complex interfaces, where the scattering can take place in regions of different density, the graded DWBA is utilized (Lazzari *et al.*, 2007; de Boer, 1996; Sentenac & Greffet, 1998). In the two-slab DWBA, four scattering amplitudes must be considered, and these are diagramed in Figs. 4(*a*)–4(*d*). The first term (*a*) is the simple Born approximation (BA), which describes conventional TSAXS data. The higher-order terms result from (*b*) the reflection of the incident beam from the interface between the two slabs followed by a scattering event, (*c*) a scattering event followed by reflection of the scattering, and (*d*) reflection of both the incident beam and the scattering. In GTSAXS, the below-horizon geometry eliminates terms where the scattering is reflected. Of the four DWBA terms, only two are allowed: (*e*) the BA term and (*f*) reflection followed by scattering. Because the reflectivity prefactors decay rapidly with incident angle ($R \propto \alpha_i^{-4}$), for sufficiently large α_i (several times the critical angle), the BA term dominates. For example, in the two-slab DWBA, the ratio of the second to first term is the reflection coefficient between the top slab and the underlying bulk. At

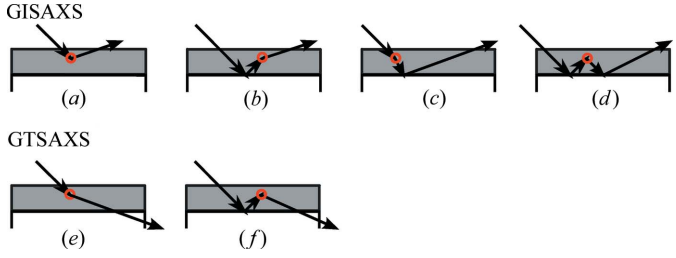

Figure 4
(*a*)–(*d*) In the two-slab DWBA, four terms contribute to the GISAXS scattering amplitude, as described in the text. (*e*), (*f*) In the two-slab DWBA only the first two terms contribute to the GTSAXS scattering amplitude. At large incident angle the scattering is well described by term (*e*) alone (Born approximation).

$\alpha_i = 0.76^\circ$ with a top-slab critical angle $\alpha_{ct} = 0.093^\circ$, the coefficient is $\sim 10^{-5}$, which will be entirely overwhelmed by the BA term. In GTSAXS, it is possible to find a regime in α_i where only the BA term is relevant but where one can still probe the relevant q_z range.

We now account quantitatively for the refraction effects, since this is required to determine the out-of-plane structure of samples. Here we introduce q'_z, the scattering vector in the top slab, and α_{ct}, the critical angle of the top interface. The electron density of the top slab relative to the substrate is $(\alpha_{ct}/\alpha_{Si})^2$. The refraction effects for the GISAXS and GTSAXS geometries are different.

In the GTSAXS geometry, the incident beam is refracted as it first enters the material from air, while the scattered beam is refracted as it enters the bulk substrate from the top slab (Fig. 1*b*). The refraction effects for the beams exiting the edge of the substrate, at nearly perpendicular angles, are negligible. The corrected scattering vector is given by

$$\begin{aligned} q'_z &= k_0\left[\left(\sin\alpha_i^2 - \sin\alpha_{ct}^2\right)^{1/2} - \left(\sin\alpha_f^2 + \sin\alpha_{Si}^2 - \sin\alpha_{ct}^2\right)^{1/2}\right] \\ &= k_0\left\{\left(\sin\alpha_i^2 - \sin\alpha_{ct}^2\right)^{1/2} \right. \\ &\quad \left. - \left[\left(q_z/k_0 - \sin\alpha_i\right)^2 + \sin\alpha_{Si}^2 - \sin\alpha_{ct}^2\right]^{1/2}\right\} \end{aligned} \quad (1)$$

for GTSAXS. As illustrated in Fig. 1(*b*), the transmitted direct beam (defined as $q'_z = 0$) is at $q_z = q_0 = k_0[\sin\alpha_i - (\sin\alpha_i^2 - \sin\alpha_{Si}^2)^{1/2}]$. In GTSAXS, the positive q_z region ranges from q_0 to $q_z = k_0 \sin\alpha_i$. As we show in the supplementary information (see supplementary Fig. 1), this formula adequately corrects the refraction of the scattered beams with $\alpha_{ct} = 0.09^\circ$ for the fingerprint-patterned sample.

In GISAXS, both the incident beam and the scattered beam are refracted at the air–film interface (Fig. 1*b*). The scattering vector in the thin film has to be corrected as

$$\begin{aligned} q'_z &= k_0\left[\left(\sin\alpha_i^2 - \sin\alpha_{ct}^2\right)^{1/2} + \left(\sin\alpha_f^2 - \sin\alpha_{ct}^2\right)^{1/2}\right] \\ &= k_0\left\{\left(\sin\alpha_i^2 - \sin\alpha_{ct}^2\right)^{1/2} + \left[\left(q_z/k_0 - \sin\alpha_i\right)^2 - \sin\alpha_{ct}^2\right]^{1/2}\right\} \end{aligned} \quad (2)$$

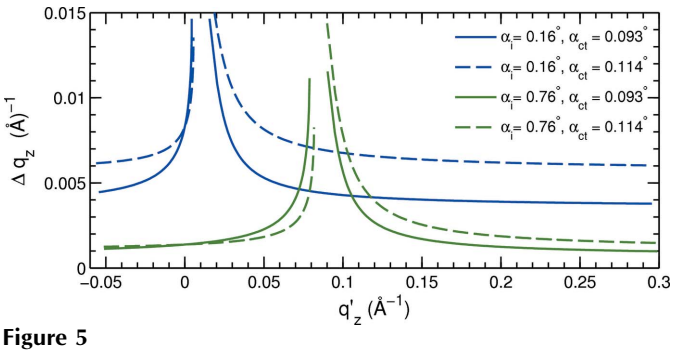

Figure 5
The displacement of the scattering vector due to the refraction effects ($\Delta q_z = q_z - q'_z$) *versus* q'_z with different incident angles [0.16° (blue) and 0.76° (green)] and different critical angles of the top slab [0.093° (solid) and 0.114° (dashed)].

for GISAXS. At small q_z the GTSAXS geometry has significantly fewer distortions than GISAXS since α_i is farther from α_{Si}.

Simple calculations using the two-slab model were carried out to illustrate the size of the refraction effects. The calculated refraction displacements of the scattering vector ($\Delta q_z = q_z - q'_z$) *versus* q'_z are shown in Fig. 5 for $\alpha_{ct} = 0.093$ and 0.114° (chosen to represent a thin film with 50 and 75% of the substrate electron density, respectively). Overall, high-α_i (green) curves require much less refraction correction than those with low α_i (blue). The figure shows a gap (a region of undefined q'_z) between the GTSAXS and GISAXS regimes, and this corresponds to the regime where $0 \le \alpha_f \le \alpha_{ct}$. The GTSAXS regime is on the left side of the gap and the GISAXS regime is on the right side of the gap, where Δq_z can be obtained from equations (1) and (2). It should be noted that refraction corrections are less sensitive to the top-layer electron density for high α_i than for low α_i. This is illustrated by Fig. 5, which shows that there is little change in the two curves with different α_{ct} for high α_i and a significant difference for low α_i. Near the gap, on either side, the refraction effects are large and vary rapidly; compensating for this distortion in data is nontrivial. The GTSAXS geometry instead pushes the distortions away from the region of interest ($q'_z \simeq 0$), with only a small and slowly varying correction remaining. This correction can be made arbitrarily small by choosing a sufficiently large incident angle. Importantly, the correction is dependent only on the (known) substrate density, since the correction becomes insensitive to the film density. The GTSAXS geometry is especially advantageous when the vertical length scale is comparable to or larger than $2\pi/q_c = \lambda/\sin\alpha_{ct}$, since many details of the BR are otherwise masked by strong refraction effects.

6. Conclusion

In conclusion, we have introduced GTSAXS as a new surface X-ray scattering method for studying nanostructured thin films. GTSAXS requires a focused beam which illuminates a region near the edge of the sample since the scattering must exit from the edge of the substrate. The incident angle for GTSAXS should be much larger than the critical angle of the substrate, in order to minimize the refraction correction, but sufficiently small in order to access the wide q_z range required to probe surface-normal structures. GTSAXS benefits from the increased scattering volume of a grazing-incidence beam projection, although not as much as with the smaller incident angles used in GISAXS. A significant advantage of GTSAXS is the ability to probe very small $|q_z|$, both for $q_z \ge 0$ and for $q_z \le 0$, a regime not accessible with GISAXS. We have demonstrated experimentally that the intensity of GTSAXS is ample for the study of gratings. A substantial advantage of GTSAXS is the straightforward analysis within the Born approximation framework. By piecing together GTSAXS data at small q_z and GISAXS data at larger q_z, where refraction effects are not severe, it should be possible to obtain surface scattering results that combine the best aspects of both

methods: straightforward Born approximation analysis along with the stronger scattering intensity at larger q_z values that GISAXS provides. GTSAXS is also a potential alternative to some direct structural probing techniques such as atomic force microscopy or SEM, especially when studying buried interfaces or performing *in situ* studies: *e.g.* wetting or non-wetting liquid fillings and resistive patterns. GTSAXS can provide statistical sampling over large areas without sample contact or damage. Because of its experimental ease and quantitative nature it should see increasing use for investigations of arrays of nanostructured objects, such as self-organized soft materials, optoelectronic elements and self-assembled templates for nanolithography.

APPENDIX *A*
Silicon nanostructure preparations

A1. Block copolymer self-assembly

We formed the polystyrene-block-polymethylmethacrylate (PS-*b*-PMMA) block copolymer thin-film patterns on silicon substrates by treating the surface with a hydroxy-terminated PS-*r*-PMMA random copolymer composed of 52:48 PS:PMMA with $M_w \simeq 11$ kg mol^{-1} (Mansky *et al.*, 1997). Films of the random copolymer were spin coated (750 r min^{-1}, 45 s) from a 0.5 wt% solution in toluene, annealed at 478 K for 3 h in vacuum (<5 Torr), rinsed in toluene and dried in a stream of dry N_2 to remove excess material. Perpendicularly oriented lamellar patterns with 48 nm periodicity were formed by spin casting a 50:50 PS:PMMA block copolymer (M_w = 104 kg mol^{-1}) from a 1 wt% solution in toluene. Block copolymer materials were purchased from Polymer Source Inc. Annealing of the block copolymer films for 3 h at 478 K in vacuum facilitates the fingerprint pattern formation (Thurn-Albrecht, 2000; Guarini *et al.*, 2002).

A2. Aluminium oxide hard mask formation

The PMMA domain of self-assembled polymer patterns was infiltrated with aluminium oxide by sequential exposure to trimethylaluminum (TMA) and water precursors in a Cambridge Nanotech Savannah 100 atomic layer deposition tool (Peng *et al.*, 2010). At a temperature of 358 K, samples were exposed to 5–10 Torr of TMA for 5 min, followed by 5 Torr of water vapor for 5 min. The process was repeated three times for each sample. Following aluminium oxide infiltration, all remaining organic material was removed by oxygen plasma (20 W, 100 mT, 60 s).

A3. Grating mask fabrication

The templates used as confining gratings consisted of ⟨100⟩-orientation p-doped Si wafers (1–12 Ω cm) fabricated by electron beam lithography using a Jeol JBX6300-FS (100 kV, 220 μC cm^{-2}, 150 pA). ZEP-520A resist (Zeon Corporation) served as a resist and etch mask.

A4. Plasma etch transfer

We transferred patterns into the underlying silicon layers with an SF_6:O_2 gas chemistry in an Oxford PlasmaLab 100 inductively coupled plasma tool operating at 15 W RF power, 800 W ICP power, 12 mTorr and 173 K (Johnston *et al.*, 2012). For lamellar pattern templates, the residual Al_2O_3 hard mask was removed using aluminium etchant (Transene Company Inc.). For lamellar pattern templates, the residual Al_2O_3 hard mask was removed using an aluminium etchant (Transene Company Inc.).

A5. Sample edge preparation

To create a clean edge the samples were scribed with a diamond tip and cleaved with a precision of about 0.5 mm. Use of higher-energy X-rays, with their larger effective footprint (*e.g.* absorption length), would decrease the sensitivity to edge defects and the sensitivity to the precise position of the cleaved edge.

This research was supported by the US Department of Energy, Basic Energy Sciences, by the Materials Sciences and Engineering Division (XL and BMO), which is supported under contract No. DE-AC02-98CH10886, and through the Center for Functional Nanomaterials (KGY, DJ and CTB), which is supported under contract No. DE-AC02-98CH10886. We thank Detlef Smilgies and Stephan Roth for productive discussions. This work was partially supported by the Energy Laboratory Research and Development Initiative at Brookhaven National Laboratories.

References

Bian, K. F., Choi, J. J., Kaushik, A., Clancy, P., Smilgies, D. M. & Hanrath, T. (2011). *ACS Nano*, **9**, 2815–2823.
Boer, D. K. G. de (1996). *Phys. Rev. B*, **53**, 6048–6064.
Busch, P., Rauscher, M., Moulin, J. & Müller-Buschbaum, T. (2011). *J. Appl. Cryst.* **44**, 370–379.
Busch, P., Rauscher, M., Smilgies, D.-M., Posselt, D. & Papadakis, C. M. (2006). *J. Appl. Cryst.* **39**, 433–442.
Doshi, D. A., Gibaud, A., Goletto, V., Lu, M., Gerung, H., Ocko, B., Han, S. M. & Brinker, C. J. (2003). *J. Am. Chem. Soc.* **125**, 11646–11655.
Guarini, K., Black, C. T. & Yeung, S. (2002). *Adv. Mater.* **14**, 1290–1294.
Guinier, A. (1994). *X-ray Diffraction in Crystals, Imperfect Crystals and Amorphous Bodies.* New York: Dover Publications.
Heitsch, A. T., Patel, R. N., Goodfellow, B. W., Smilgies, D. M. & Korgel, B. A. (2010). *J. Phys. Chem. C*, **114**, 14427–14432.
Hlaing, H., Lu, X., Hofmann, T., Yager, K. G., Black, C. T. & Ocko, B. M. (2011). *ACS Nano*, **5**, 7532–7538.
Hlaing, H., Lu, X., Nam, C.-Y. & Ocko, B. M. (2012). *Small.* **8**, 3443–3447.
Hofmann, T., Dobisz, E. & Ocko, B. M. (2009). *J. Vacuum Sci. Technol. B*, **27**, 3238–3243.
Hu, T., Jones, R. L., Wu, W., Lin, E. K., Lin, Q., Keane, D., Weigand, S. & Quintana, J. (2004). *J. Appl. Phys.* **96**, 1983–1987.
Jiang, Z., Lee, D. R., Narayanan, S., Wang, J. & Sinha, S. K. (2011). *Phys. Rev. B*, **84**, 075440.
Johnston, D. E., Lu, M. & Black, C. T. (2012). *Proc. SPIE*, **8328**, 83280A.

Jones, R. L., Hu, T., Lin, E. K., Wu, W.-L., Kolb, R., Casa, D. M., Bolton, P. J. & Barclay, G. C. (2003). *Appl. Phys. Lett.* **83**, 4059–4061.
Lazzari, R., Leroy, F. & Renaud, G. (2007). *Phys. Rev. B*, **76**, 125411.
Lee, B., Park, I., Park, H., Lo, C.-T., Chang, T. & Winans, R. E. (2007). *J. Appl. Cryst.* **40**, 496–504.
Lee, B., Park, I., Yoon, J., Park, S., Kim, J., Kim, K.-W., Chang, T. & Ree, M. (2005). *Macromolecules*, **38**, 4311–4323.
Levine, J. R., Cohen, J. B., Chung, Y. W. & Georgopoulos, P. (1989). *J. Appl. Cryst.* **22**, 528–532.
Lin, Y., Böker, A., Skaff, H., Cookson, D., Dinsmore, A. D., Emrick, T. & Russell, T. P. (2005). *Langmuir*, **21**, 191–194.
Mansky, P., Liu, Y., Huang, E., Russell, T. P. & Hawker, C. (1997). *Science*, **275**, 1458–1460.
Papadakis, C., Di, Z., Posselt, D. & Smilgies, D.-M. (2008). *Langmuir*, **24**, 13815–13818.
Park, S., Lee, D. Y., Xu, J., Kim, B., Hong, S. W., Jeong, U., Xu, T. & Russell, T. P. (2009). *Science*, **323**, 1030–1033.
Peng, Q., Tseng, Y. C., Darling, S. B. & Elam, J. W. (2010). *Adv. Mater.* **22**, 5129–5133.
Rauscher, M., Paniago, R., Metzger, H., Kovats, Z., Domke, J., Peisl, J., Pfannes, H.-D., Schulze, J. & Eisele, I. (1999). *J. Appl. Phys.* **86**, 6763–6769.
Rauscher, M., Salditt, T. & Spohn, H. (1995). *Phys. Rev. B*, **52**, 16855–16863.
Renaud, G., Lazzari, G. R. & Leroy, F. (2009). *Surf. Sci. Rep.* **64**, 255–380.
Roth, S. V., Autenrieth, T., Grübel, G., Riekel, C., Burghammer, M., Hengstler, R., Schulz, L. & Müller-Buschbaum, P. (2007). *Appl. Phys. Lett.* **91**, 091915.
Roth, S. V., Burghammer, M., Riekel, C., Müller-Buschbaum, P., Diethert, A., Panagiotou, P. & Walter, H. (2003). *Appl. Phys. Lett.* **82**, 1935–1937.
Roth, S. V., Herzog, G. *et al.* (2011). *J. Phys. Condens. Matter*, **23**, 254208.
Roth, S. V., Kuhlmann, M., Walter, H., Snigirev, A., Snigireva, I., Lengeler, B., Schroer, C. G., Burghammer, M., Riekel, C. & Müller-Buschbaum, P. (2009). *J. Phys. Condens. Matter*, **21**, 264012.
Rueda, D. R., Martín-Fabiani, I., Soccio, M., Alayo, N., Pérez-Murano, F., Rebollar, E., García-Gutiérrez, M. C., Castillejo, M. & Ezquerra, T. A. (2012). *J. Appl. Cryst.* **45**, 1038–1045.
Sentenac, A. & Greffet, J.-J. (1998). *J. Opt. Soc. Am. A*, **15**, 528–532.
Sinha, S. K., Sirota, E. B., Garoff, S. & Stanley, H. B. (1988). *Phys. Rev. B*, **38**, 2297–2311.
Smilgies, D. M., Heitsch, A. T. & Korgel, B. A. (2012). *J. Phys. Chem. C*, **116**, 6017–6026.
Tate, M. P., Urade, V. N., Kowalski, J. D., Wei, T.-C., Hamilton, B. D., Eggiman, B. W. & Hillhouse, H. W. (2006). *J. Phys. Chem. B*, **110**, 9882–9892.
Thurn-Albrecht, T. R., Steiner, R., DeRouchey, J., Stafford, C. M., Huang, E., Bal, M., Tuominen, M., Hawker, C. J. & Russell, T. P. (2000). *Adv. Mater.* **12**, 787–791.
Urban, J. J., Talapin, D. V., Shevchenko, E. V. & Murray, B. C. (2006). *J. Am. Chem. Soc.* **128**, 3248–3255.
Vineyard, G. H. (1982). *Phys. Rev. B*, **26**, 4146–4159.
Yan, M. & Gibaud, A. (2007). *J. Appl. Cryst.* **40**, 1050–1055.
Yan, R. E. G. & Yang, P. (2009). *Nat. Photon.* **3**, 569–576.
Yoneda, Y. (1963). *Phys. Rev.* **131**, 2010–2013.
Zhang, J., Luo, Z., Martens, B., Quan, Z., Kumbhar, A., Porter, N., Wang, Y., Smilgies, D.-M. & Fang, J. (2012). *J. Am. Chem. Soc.* **134**, 14043–14049.